Electronic Supplementary Information (ESI)

A palm-size μNMR relaxometer using a digital microfluidic device and a semiconductor transceiver for chemical/biological diagnosis

Ka-Meng Lei,[ab] **Pui-In Mak,**[*ab] **Man-Kay Law,**[a] **and Rui P. Martins**[abc]

[a] State-Key Laboratory of Analog and Mixed-Signal VLSI, University of Macau, China

[b] Faculty of Science and Technology, Dept. of ECE, University of Macau, China

[c] On leave from Instituto Superior Técnico, Universidade de Lisboa, Portugal

* E-mail: pimak@umac.mo

1. Highlight of recent µNMR systems

Recent advancement of the µNMR system including their overall illustration together with the picture of the integrated circuits are shown in Fig. S1. This work succeeds in managing multiple samples under NMR assay using electronic-automated method which can decrease amount of labor work (error) and the risks of defilement.

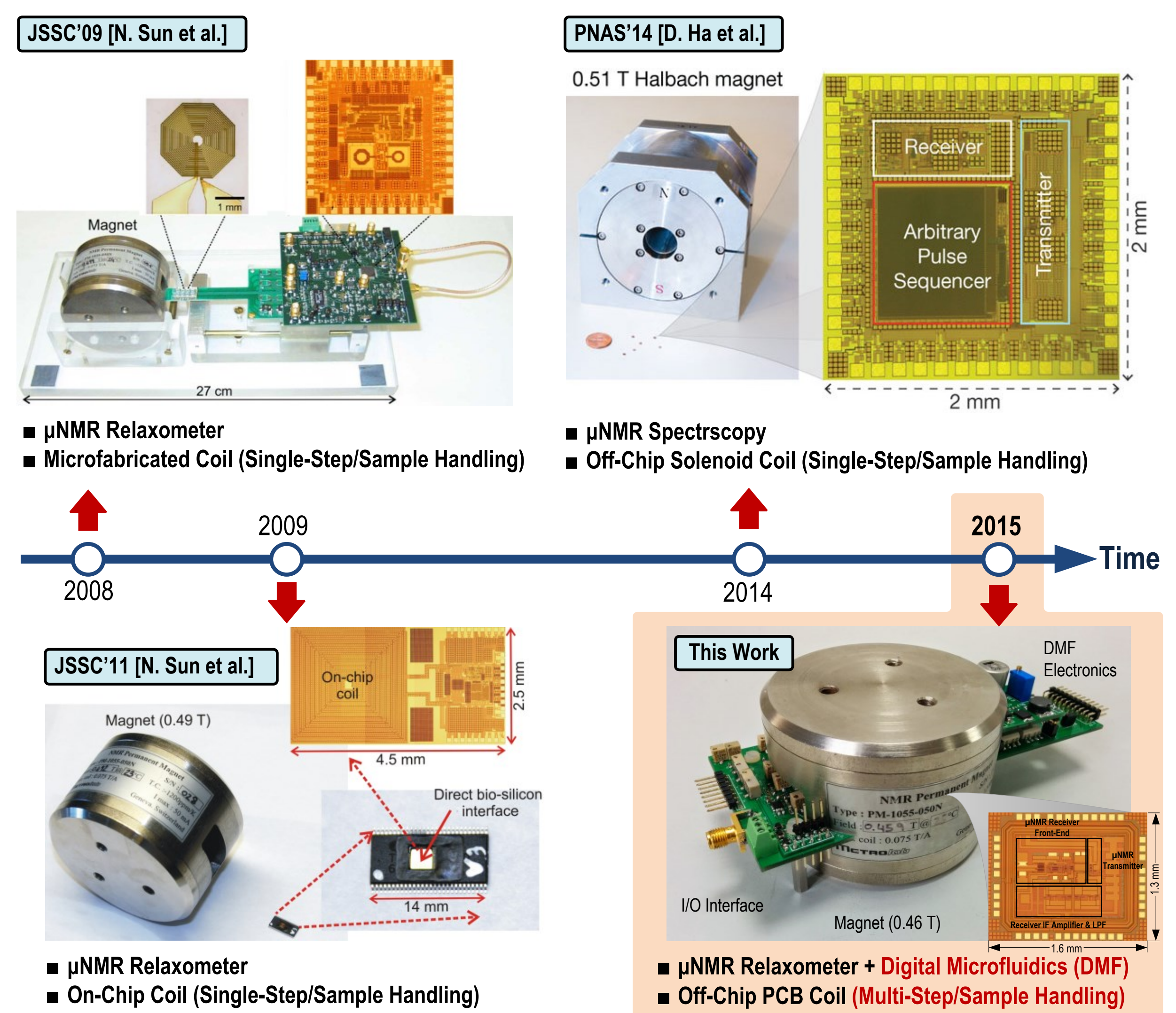

Fig. S1 µNMR systems developed in the last decade. This work succeeds in integrating the DMF device into the µNMR relaxometer to achieve multi-step multi-sample handling inside a volume-limited portable magnet.

2. Design of the CMOS μNMR Transceiver

The semiconductor transceiver for μNMR-signal excitation and reception was designed and fabricated in a 0.18-μm CMOS technology to optimize the overall performance and integration level. As depicted in Fig. S2, there are two parts: transmitter and receiver, as detailed below.

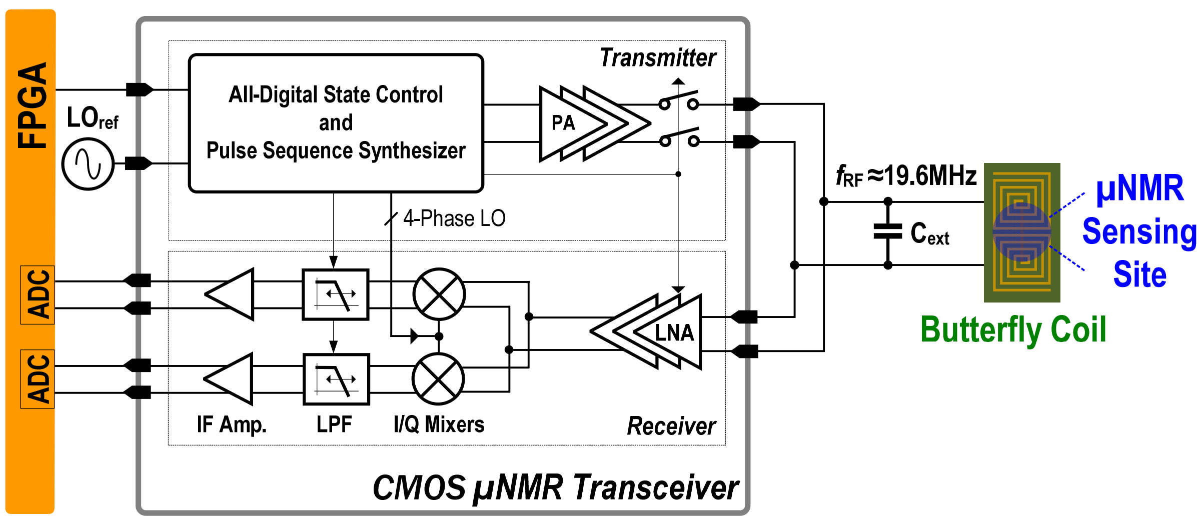

Fig. S2 Schematic of the μNMR transceiver and its connection to the external parts including the Butterfly coil.

2A. Transmitter

The transmitter generates the Carr-Purcell-Meiboom-Gill pulse sequence and delivers adequate signal power to the external Butterfly coil to excite the nuclei of the droplet sample. An all-digital state control and a pulse sequence synthesizer are integrated to read the commands given from the field programmable gate array (FPGA). The FPGA manages the overall status of the transceiver, including the low-noise amplifier (LNA) stage, transmission switches, and low-pass filters (LPFs). In addition, the synthesizer will control the pulse sequence that is delivered to the power amplifier (PA) with proper phase (0º or 90º), which is synthesized from the external

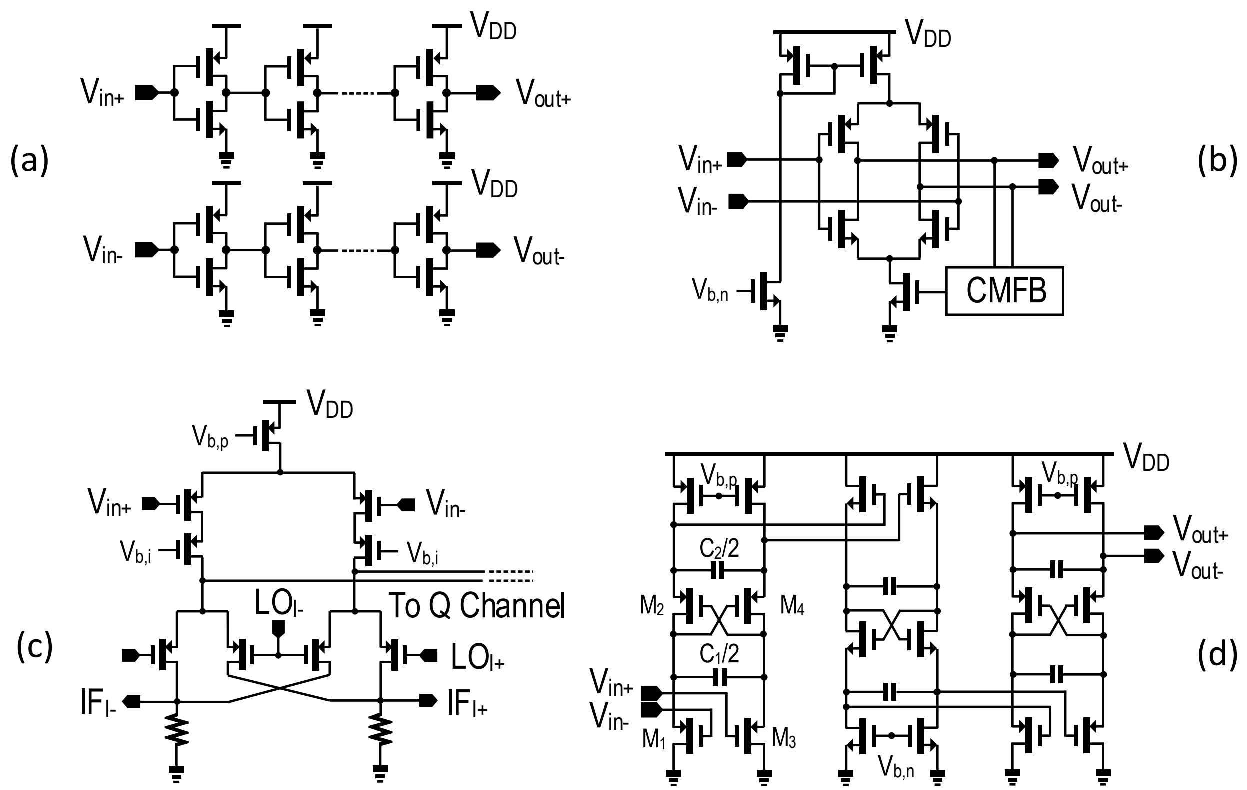

Fig. S3 Schematics of the key functional blocks: (a) power-efficient multi-stage inverter-based PA; (b) NMOS-PMOS differential-pair LNA with high gain and low noise; (c) I/Q active mixers with common PMOS differential pair for noise reduction; (d) area-efficient and high-linearity 6th-order source-follower-based LPF.

reference signal LO_{ref}. The PA, as shown in Fig. S3(a), is realized as a differential chain of four inverter stages to optimize the output current driving to the Butterfly coil, while reducing the propagation delay. The size of the inverters is quadrupled sequentially to boost the output power. This class-D PA topology does not consume static current, resulting in better power efficiency. The switches controlled by the state control were inserted between the PA and the Butterfly coil. The Butterfly coil is tailored to enlarge the usability space inside the portable magnet.

2B. Receiver

The receiver is to extract the weak μNMR signal induced by the Butterfly coil from the protons. Outside the transceiver chip, a discrete capacitor C_{ext} is placed in parallel with the Butterfly coil for resonant pre-filtering, while offering a passive pre-gain to the signal.[S1] This is a feasible technique as the received signal is narrowband around the Larmor frequency, thus no distortion will be added. Inside the chip, the receiver is headed by a multi-stage LNA as shown in Fig. S3(b). It dominates the signal-to-noise ratio of the receiver, as the noise contribute from the subsequent stages will be suppressed by the gain of it. The LNA is optimized for low noise to avoid deteriorating the signal-to-noise ratio of the μNMR signal, whereas it should avoid immense power unsuitable for point-of-care diagnostic tools. This work uses a complementary common-source topology for current reuse, which provides better performances when compared with the typical common-source amplifier. The differential implementation rejects the common-mode noises picked from the environments (i.e., electromagnetic interference and power line coupling). A common-mode feedback (CMFB) circuit stabilizes the output common-mode level. Three similar LNAs are cascaded to amplify the signal for subsequent signal processing.

The LNA is followed by two active mixers for I and Q channels, as shown in Fig. S3(c), for downconverting the radio-frequency (RF) signal at 19.6 MHz to intermediate frequency (IF) signal at ~1 kHz for digitization. The mixers are double-balanced to reduce the noise figure (double sideband) and feedthrough from the local oscillator (LO) to the IF. The 4-phase LO is provided by the pulse sequence synthesizer. The mixers are constructed by PMOS transistors to reduce the flicker noise and substrate coupling from/to another part of the chip.

The downconverted μNMR signal will be further processed by the LPFs, which suppress the out-of-band noise and unwanted high-frequency products generated by the hard-switched mixing process. The LPFs are implemented as a 6th-order Butterworth using the source-follower-based topology, visualized in Fig. S3(d).[S2] Such topology features a transistorized positive-feedback technique to build a complex pole in a single branch, reducing the circuit complexity and unwanted parasitic poles. Assuming M_1 and M_3 have a transconductance g_{m1}, and M_2 and M_4 have a transconductance g_{m2}, the transfer function and corresponding cut-off frequency of each Biquad are given by:

$$H(s) = \frac{1}{s^2 \frac{C_1 C_2}{g_{m1} g_{m2}} + s \frac{C_2 g_{m1} - C_2 g_{m2} + C_1 g_{m2}}{g_{m1} g_{m2}} + 1} \tag{S1}$$

$$\omega_0 = 2\pi f_0 = \sqrt{\frac{g_{m1} g_{m2}}{C_1 C_2}} \tag{S2}$$

As g_m of the transistor is proportional to the square root of its bias current, the cutoff frequency can be adjusted by controlling the bias current. This aim avoids the use of large resistors or capacitors which are costly in integrated circuits. In addition, unlike the fixed-resistor-capacitor LPFs, the bandwidth of this kind of LPF is tunable by altering the bias current of the transistors, being more area-efficient for bandwidth control. Two PMOS-type Biquad and one NMOS-type Biquad are cascaded to construct the 6th-order Butterworth response, while matching their input and output common-mode levels.

The selected LPF's bandwidth is critical to the quality of the final received μNMR signal. Excess bandwidth will raise the out-of-band noise, but inadequate bandwidth will distort the signal thus penalizing the result accuracy. The excitation pulses will affect the output DC level, and thus it will affect also the DC level of the following echo signals and distort the result.

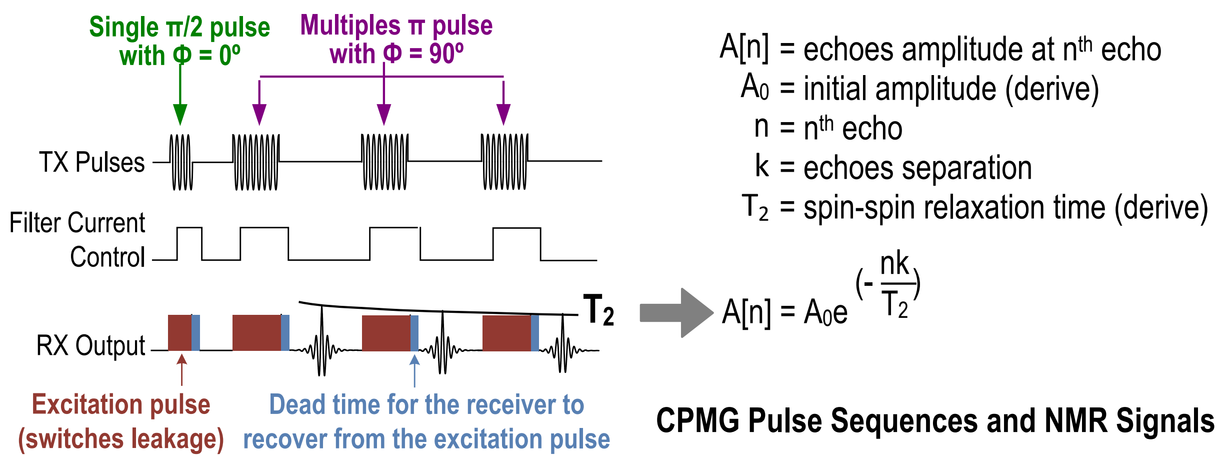

Fig. S4 Timing diagram of the CPMG pulse sequences and the receiver output response showing the dead time of the receiver caused by the excitation pulses. Echoes amplitude of the NMR signals is also shown in the figure.

As shown in Fig. S4, even there are isolation switches to prevent the excitation pulses from saturating the receiver, there are still leaking pulses appear at the output due to non-ideal switches, causing a dead time for the receiver. Yet, with a small bias current, the duration of recovery from the dead time caused by the excitation pulse will be longer. Simulated in MATLAB, the step responses of an ideal 6^{th}-order Butterworth LPF with a bandwidth from 2 to 10 kHz are shown in Fig. S5, where the inset shows the settling time of the LPF at different cutoff frequencies. The settling time is inversely proportional to the cutoff frequency, posing a tight trade-off between the receiver's noise and settling time if the bandwidth is fixed. Herein we proposed a dynamic-bandwidth LPF topology to break such a trade-off. As shown in Fig. S4, the bandwidth of the LPF is expanded during the excitation mode to swiftly recover from the excitation pulse, while its bandwidth is shrunk in the stable receiving mode to reduce the out-of-band noise.

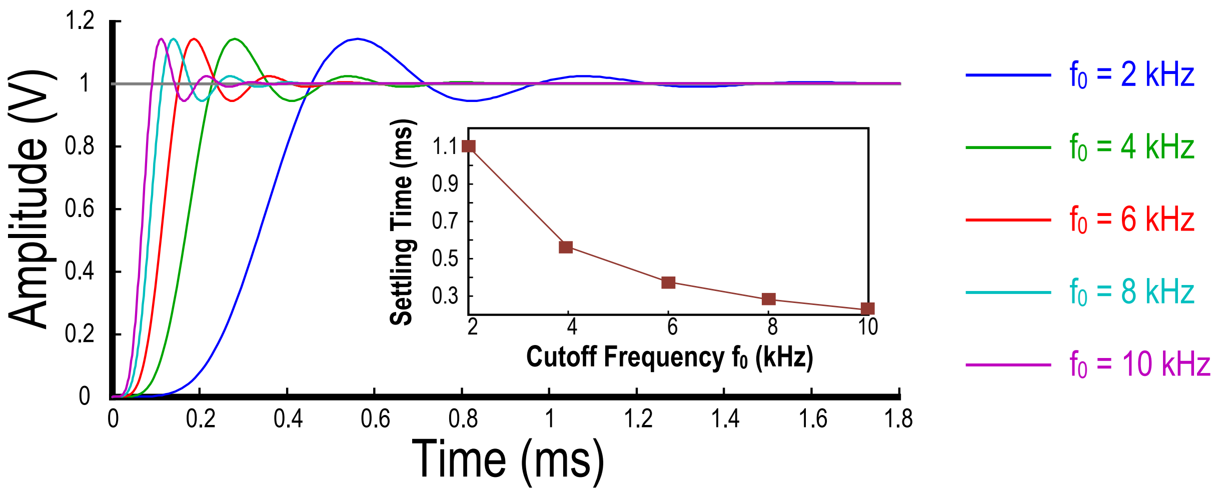

Fig. S5 The step response of the 6th-order Butterworth LPF with different cut-off frequencies f_0. Inset shows the corresponding settling times.

Subsequent to the LPFs, voltage buffers implemented as a simple source-degenerative common-source amplifier with a gain of 2 V/V are adopted to drive the off-chip analog-to-digital converters, which are enclosed within the FPGA board for digitization.

3. Simulation and Measurement Results of the CMOS Transceiver

The CMOS transceiver is power-up via low-dropout regulators ADP323 from Analog Devices Inc. (Norwood, MA) and current regulators LM334 from Texas Instruments Inc. (Dallas, TX). Measurement results show the transmitter draws 19.6 mW power in transmitting mode, whereas the PA dominates the power consumption (>99%). The PA has a high power efficiency of 28% and provides an effective RF field of 5.7 Gauss on the samples.

The receiver has a simulated gain of 87.6 dB at 20 MHz with an input-referred noise of 0.92 nV/√Hz for each channel. The measured power consumption of the receiver is 26.6 mW, with the forefront LNA consumes prodigious power (18.0 mW), as a large bias current is entailed to suppress the noise.

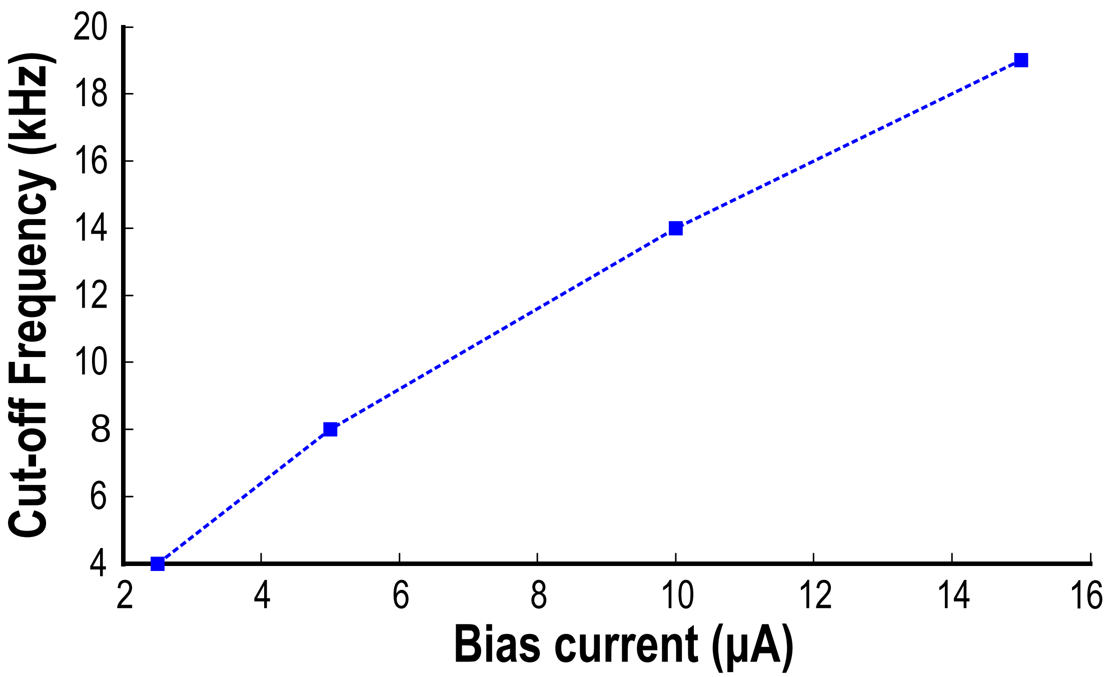

Fig. S6 The relationship between the LPF's cut-off frequency and its bias current.

The bandwidth of the LPF versus the bias current is measured as shown in Fig. S6. With a large bias current, the g_m of the transistors will be raised up, causing the cut-off frequency of the LPF to be increased as predicted in Eqn. (S2). Thus, the dynamic-bandwidth tuning can be achieved by altering the bias current of the LPFs during the excitation and receiving modes. This method can preserve a low out-of-band noise while shortening the effect of the switch leakages during the excitation mode.

4. Co-optimization of the butterfly coil and CMOS transceiver

The geometry (i.e., number of turns) for the Butterfly coil is closely related to the SNR of the μNMR receiver. The induced voltage V_{EMF} of the coil can be expressed as:

$$V_{\mathrm{EMF}} = -\int \left(\frac{\partial}{\partial t}\right)(B_1 M_0)\, dV_s \tag{S3}$$

with the nuclear magnetization M_0, the RF magnetic field produced by the unit current passing through the Butterfly coil B_1 and the volume of the droplet V_S. V_{EMF} of the different Butterfly coils thus can be compared by averaging B_1 acting on the droplets provided that the magnetization of the nuclei and the volume and shape of the droplet are the same for both cases. Consequently, the thermal noise for the conductor of the Butterfly coil can be expressed by the Nyquist formula:

$$\overline{V^2{}_{noise,coil}} = 4k_B T_{coil} R_{coil} \tag{S4}$$

with the Boltzmann's constant k_B, the resistance of the Butterfly coil path R_{coil} and absolute temperature of the conductor T_{coil}. Both of the induced voltage and thermal noise are amplified with a passive gain $\sqrt{Q^2+1}$ offered by the LC-tank where Q is the quality factor of the Butterfly coil. Depicted in Fig. S7(a), the SNR appear at the output of the receiver can be expressed as:

$$SNR = \frac{V_{\mathrm{EMF}}\sqrt{Q^2+1}}{\sqrt{\overline{V^2{}_{noise,coil}}(Q^2+1) + \overline{V^2{}_{noise,rec}}}} \tag{S5}$$

Deduced from eqn. (S5), the SNR of the μNMR receiver is a function of Butterfly coil geometry (V_{EMF}, $\overline{V^2{}_{noise,coil}}$ and Q) as well as receiver noise ($\overline{V^2{}_{noise,rec}}$). With a fix budget of

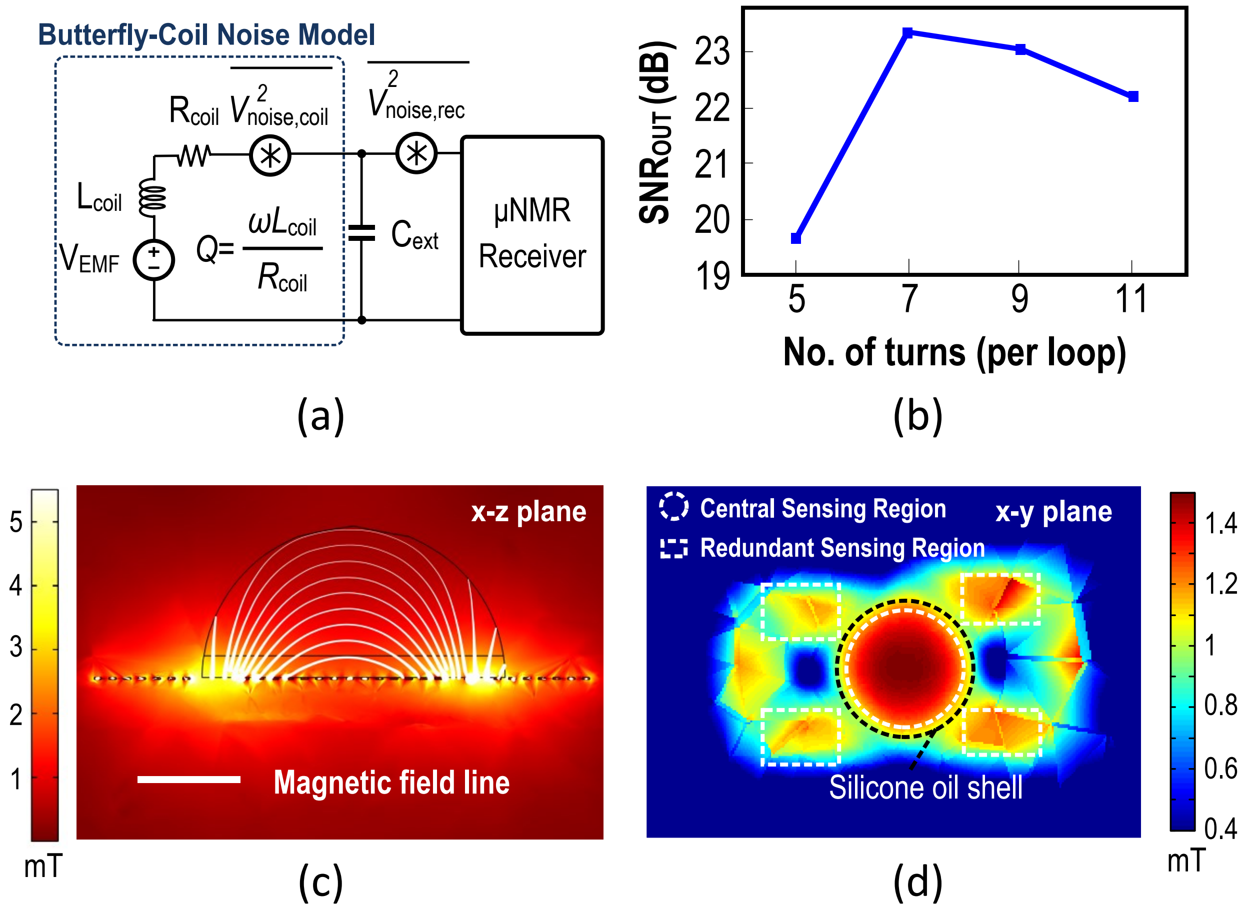

Fig. S7 (a) Noise equivalent circuit of the receiver front-end with the Butterfly coil. (b) The SNR of the µNMR receiver versus the number of turns of the Butterfly coil with a receiver input referred noise of 0.92 nV/√Hz. An optimal number of turns of 7 is obtained by multi-domain simulation. (c) The magnetic field pattern of the 7-turn Butterfly coil in x-z plane. The RF magnetic field in the center of the Butterfly coil goes in x-direction. (d) The magnetic field pattern of the Butterfly coil in x-y plane. The center of the Butterfly coil has strongest magnetic field strength with some redundant sensing region.

receiver noise (limited by the semiconductor process and power), the SNR of the µNMR receiver depends on the coil geometry, necessitating systematic study and optimization involving the finite element analysis simulator and electronic circuit simulations.

Butterfly coils with different number of turns (5, 7, 9, 11 turns on each spiral) were studied in COMSOL Multiphysics® including their resistances, inductances and RF-magnetic field pattern. With simulated receiver noise of 0.92 nV/√Hz, the SNR of distinct Butterfly-coil-input CMOS transceiver are plotted in Fig. S7(b). The derived optimum number of turns for the Butterfly coil is 7 and it is adopted in the μNMR relaxometer. Table S1 summarizes the characteristics of the Butterfly coils.

Table S1 Simulated parameters of the Butterfly coil with distinct number of turns per spiral @ 20 MHz.

Turns	Resistance (Ω)	Inductance (nH)	Q	$\overline{B_1}$ (mT)
5	0.795	167.4	26.5	0.292
7	1.486	354.8	30.0	0.596
9	2.61046	668.5	32.2	0.891
11	4.12017	1144.4	34.9	1.190

The magnetic field pattern of the resultant 7-turn Butterfly coil is also demonstrated. The magnetic field in x-z plane and its direction is illustrated in Fig. S7(c). Within the center of the Butterfly coil, the RF magnetic field mainly passes through in x-direction, thus orthogonal to the static magnetic field (z-direction). Fig. S7(d) depicts the magnetic field in x-y plane. The center region of the Butterfly coil has the strongest magnetic field peaking the μNMR strength, making it suitable for μNMR sensing. Yet, it is surrounded by some redundant sensing regions that may affect the results if they are filled with oil. Explained in the subsequent section, the use of a thin shell of oil applied to each droplet implies that the minimal overlap of the silicone oil with the redundant regions induces negligible effect.

5. Digital Microfluidic Module

The simplified schematic of the digital microfluidic (DMF) module is shown in Fig. S8. A step-up voltage-to-voltage boost converter was used to built-up with LM3478 switching controller from Texas Instruments Inc. to generate a sufficiently-high voltage signal for electrode actuation. The input power is directly drawn from the FPGA board at 5 V; this act avoids the need of another high-voltage supply for better portability.

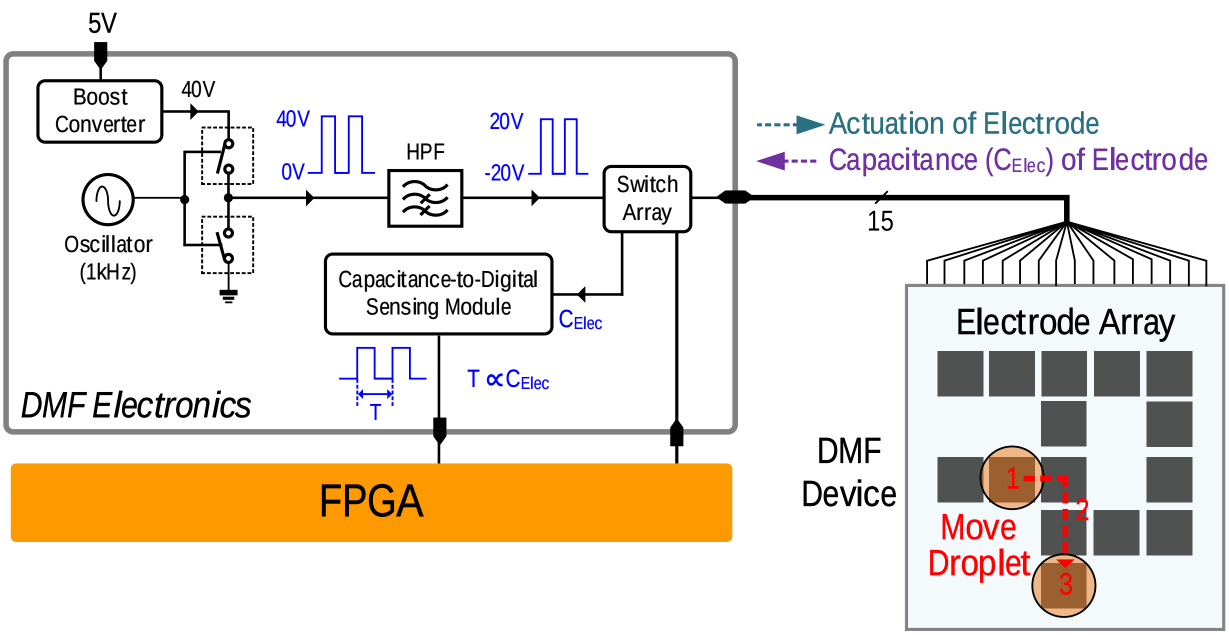

Fig. S8 Schematic of the DMF module.

An oscillator built up with timer ICM7555 from Intersil (Milpitas, CA) is used to generate a square wave of 1 kHz. This square wave is amplified into a 40-V peak-to-peak voltage by a switch pair, and then high-pass filtered to remove the DC level for actuating the electrodes. A switch array mastered by the FPGA was used to control the on-off pattern of the electrodes. To reduce the RMS-voltage stress on the electrode so as to minimize the chance of dielectric breakdown, the driving voltage on an occupied electrode is modulated with on (off) duty cycle of 10% (90%). Exemplified in Fig. S9, after continuous square wave of 3 s acting on the electrode, the pulse acting on the electrode with droplet is modulated with a turn on-off pattern of 1 to 9. This modulation technique allows the electrode to strap the droplet and prevents the dielectric breakdown of the electrode caused by the long-term voltage stress.

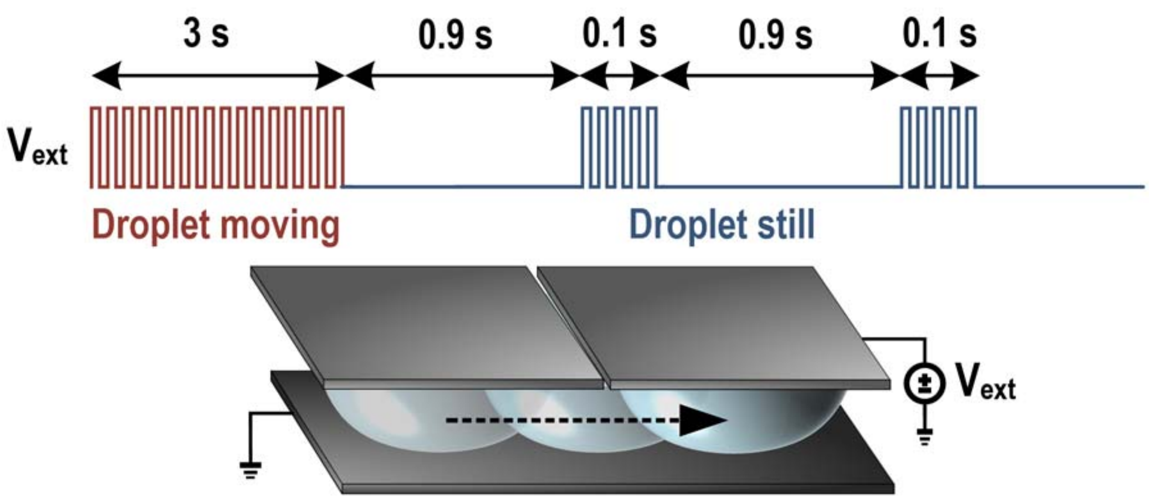

Fig. S9 Visualized waveform applied on the electrode before and after the droplet arrives the electrode.

The location of each droplet sample is determined by scanning the derived capacitance C_{elec} of each electrode. As the capacitance between two parallel plates is proportional to the permittivity of its insulating medium, a droplet-occupied electrode will increase the capacitance on the corresponding electrode when compared with the air. In this work, a timer ICM7555 working in the astable mode is used to sense the electrode capacitance. The oscillation frequency of the timer is inversely proportional to the capacitance. Thus, the identification of droplet position can be done by counting the pulses available in a fixed period of time on each electrode.

6. DMF Device Fabrication

The fabrication procedure of the DMF device including the top plate and bottom plate is shown in Fig. S10.

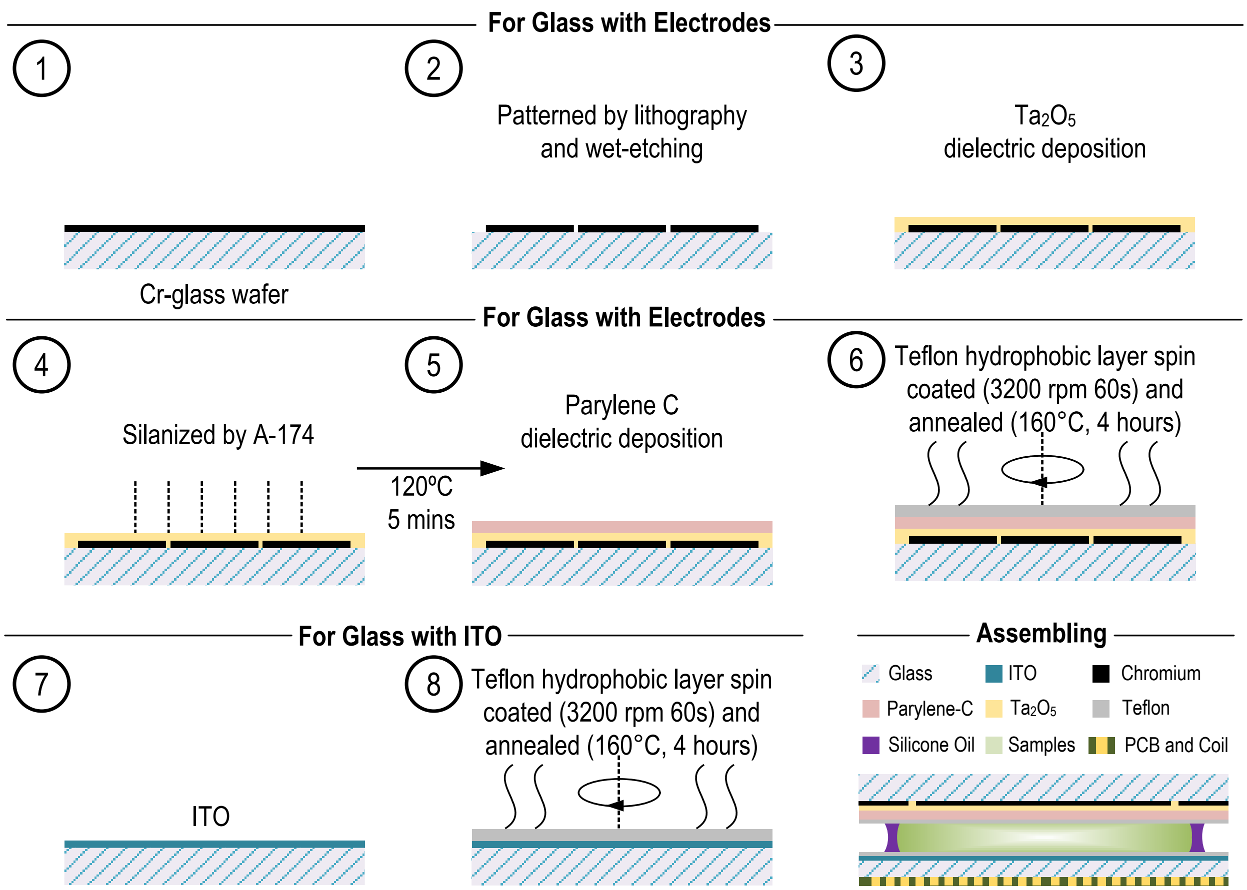

Fig. S10 Fabrication procedure of Ta_2O_5/Parylene C-insulated DMF device. Step 1 to 6 shows the fabrication process of the plate with electrode while the fabrication process of the plate with ITO is shown in step 7 to 8. The Assembly of the DMF device together with the Butterfly coil is also shown in the figure.

1. The patterns of the electrode array were drawn in AutoCad and the mask with the designed patterns is prepared for lithography on the Cr-coated glass.
2. The patterns were etched on the glass with standard lithography and wet-etch methods.

3. Dielectric layer Ta_2O_5 was deposited on the glass by reactive DC magnetron sputtering (HHV, Auto 500) at room temperature with 99.99% Ta target under an Ar/O_2 ambient. The chamber pressure was then decompressed to 1.3 x 10^{-4} Pa and back filled with sputtering gas with 15 sccm Ar and 2.05 sccm O_2 with power of 110 W and deposition rate of 2.4 nm/min. The thickness of Ta_2O_5 layer is 250 nm. In order to suppress the number of pin-holes in the dielectric, the oxidized layer was thermal annealed immediately in N_2 atmosphere at 400 ºC for 10 mins.
4. Silquest A-174 Silane solution from Momentive Performance Materials Inc. (Columbus OH) was adopt to prime the surface of the chip in isopropyl alcohol for 15 mins to strengthen the adhesion between Ta_2O_5 and Parylene C coatings, which is coated on the chip later. The glass was then baked at 120 ºC for 5 mins.
5. Parylene-C layer, which is used to screen the pinholes in Ta_2O_5 layer and prevent exposure of Ta_2O_5 to liquid samples while maintaining the high dielectric constant and strength of the Ta_2O_5, was deposited atop Ta_2O_5 surface by low pressure chemical vapor deposition method carrying out in LH300 from La-Chi Enterprise Co., Ltd. (Taiwan).
6. Amorphous fluoropolymer hydrophobic layers (100 nm) was formed by spin coating 0.5% Teflon® AF 1601S from Dupont (Wilmington, DE) in perfluorosilane FC-40 from 3M Co. (St. Paul, MN) at 3200 rotation per minute (rpm) for 60 s. Then the glass was treated at 160 °C for 4 hours.
7. ITO coated glass was prepared which functions as a ground node for all the electrodes.
8. Amorphous fluoropolymer hydrophobic layers (100 nm) was formed on the ITO coated glass by spin coating 0.5% Teflon® AF 1601S from Dupont in perfluorosilane FC-40 from 3M Co. at 3200 rpm for 60 s. Then the glass was treated at 160 °C for 4 hours.

The assembly of the resulted DMF device together with the Butterfly coil fabricated on the PCB is shown in Fig. S10.

7. Droplet Actuation

The snapshots of a droplet transported from one electrode to its neighbor are shown in Fig. S11(a)-(h). The droplet is at rest first. When a 40-V_{pp} square wave was applied to a neighboring electrode, the droplet moves toward the actuating electrode gradually. The entire movement takes around 3 s, equivalent to an average velocity of 1.17 mm/s.

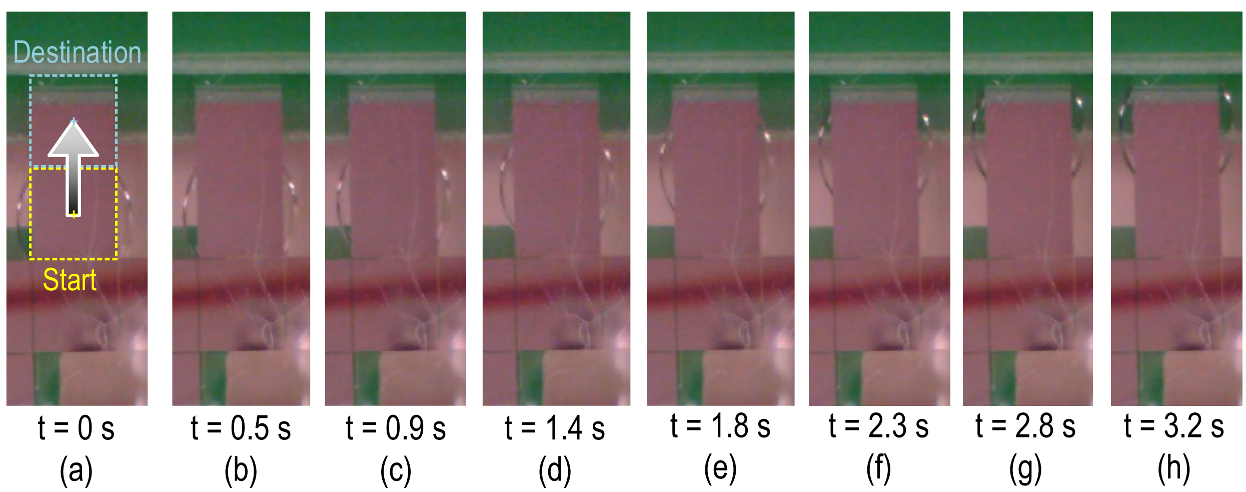

Fig. S11 (a)-(h) Snapshots of the DMF device transporting the droplets from t = 0 s to t = 3.2 s. At t = 0 s, the square wave was applied to the neighboring electrode, causing the surface tension of the droplet near the electrode changed and attracted the droplet.

8. μNMR Relaxometer Software and Hardware Interfaces

To facilitate the setting of μNMR parameters and route optimization of DMF, a graphic-user-interface program implemented in Visual C# was adopted to master the whole μNMR relaxometer includes: i) setting the μNMR parameters; ii) displaying the μNMR results; iii) reading the ambient temperature and calibrating the DAC output; iv) controlling the switch array for the DMF device, and v) displaying the vacancy of the electrodes. To achieve this, an interface is entailed for communications between the FPGA (for hardware control) and the PC (for software computing).

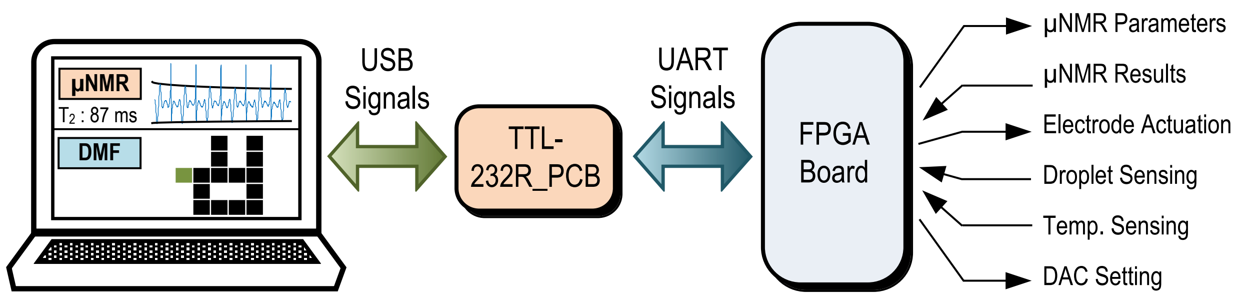

Fig. S12 The communication between the PC and the FPGA board to drive the μNMR relaxometer. It is done by adopting the TTL-232R_PCB module to interfacing between the PC and FPGA board, which mastered the hardware of the μNMR relaxometer.

The TTL-232R_PCB module from Future Technology Devices International Limited (United Kingdom) is used for interfacing between the PC and FPGA board. It can read/transmit data from/to FPGA board using the UART (universal asynchronous receiver/transmitter) signals, and the PC will process the data from the module. This protocol can ease the design for both hardware and software levels. As shown in Fig. S12, the PC sends data to the FPGA using the TTL-232R_PCB module with a unique address. The module will process the command and convert it to a readable format for the FPGA. The FPGA board with a defined address will send the corresponding command to the appropriate module. For instance, if the PC set one of the electrode to “ON” state for the DMF device, the FPGA will recognize this command and set the corresponding output to a high level, which will set the accompanying switch and drive the electrode for droplet actuation. With the PC, all the necessary control of the μNMR relaxometer can be simplified into the software level. This can eliminate the use of cumbersome hardware such as digital logics and switches, providing a neat platform for controlling the μNMR relaxometer.

References

[S1] N. Sun, T-J. Yoon, H. Lee, W. Andress, R. Weissleder and D. Ham, *IEEE J. Solid-State Circuits*, 2011, 46(1), 342-352.

[S2] S. D'Amico, M. Conta and A. Baschirotto, *IEEE J. of Solid-State Circuits*, 2006, 41(12), 2713-2719.